



Inter-calibration of SAR data series for offshore wind resource assessment

Badger, Merete; Ahsbahs, Tobias Torben; Maule, Petr; Karagali, Ioanna

Published in:
Remote Sensing of Environment

Link to article, DOI:
[10.1016/j.rse.2019.111316](https://doi.org/10.1016/j.rse.2019.111316)

Publication date:
2019

Document Version
Peer reviewed version

[Link back to DTU Orbit](#)

Citation (APA):
Badger, M., Ahsbahs, T. T., Maule, P., & Karagali, I. (2019). Inter-calibration of SAR data series for offshore wind resource assessment. *Remote Sensing of Environment*, 232, Article 111316.
<https://doi.org/10.1016/j.rse.2019.111316>

General rights

Copyright and moral rights for the publications made accessible in the public portal are retained by the authors and/or other copyright owners and it is a condition of accessing publications that users recognise and abide by the legal requirements associated with these rights.

- Users may download and print one copy of any publication from the public portal for the purpose of private study or research.
- You may not further distribute the material or use it for any profit-making activity or commercial gain
- You may freely distribute the URL identifying the publication in the public portal

If you believe that this document breaches copyright please contact us providing details, and we will remove access to the work immediately and investigate your claim.

1 Inter-calibration of SAR data series for offshore wind resource assessment

2
3 Merete Badger^{a*}, Tobias Ahsbals^a, Petr Maule^a, Ioanna Karagali^a

4
5 ^aTechnical University of Denmark, Department of Wind Energy, Frederiksborgvej 399, 4000

6 Roskilde, Denmark, e-mail mebc@dtu.dk

7 *Corresponding author

8
9 Highlights

- 10 • Offshore wind resource assessment requires long-term wind data records.
- 11 • Wind speed retrievals from different European SAR sensors are offset.
- 12 • Biases vary over time and according to scan modes and incidence angles.
- 13 • Inter-calibration can remove biases and improve the accuracy on wind resources.

14
15 Abstract

16 Wind observations in the marine environment are both costly and sparse. This makes wind
17 retrievals from satellite Synthetic Aperture Radar (SAR) an attractive option in connection
18 with planning of offshore wind farms. Because the wind power density is proportional to the
19 wind speed cubed, it is important to achieve the highest possible absolute accuracy on SAR
20 wind speed retrievals for wind energy applications. A method is presented for inter-
21 calibration of SAR observations from Envisat and Sentinel-1A/B. Sensor-specific effects on
22 the SAR-retrieved wind speeds are first quantified through comparisons against collocated
23 ocean buoy observations. Based on global circulation model simulations of wind speed and
24 direction, we retrieve the Normalized Radar Cross Section (NRCS) for different radar
25 incidence angles. Residuals between the retrieved and the observed NRCS are used to inter-
26 calibrate the observed NRCS before reprocessing to SAR wind fields. The inter-calibration

27 leads to an improved agreement between SAR and buoy wind speeds with biases below 0.2 m
28 s⁻¹ for all investigated SAR sensors. Estimates of the wind resource improve with respect to
29 the buoy observations for ten of the twelve sites investigated. The average deviation between
30 wind power densities is reduced from 20% to 8% as the SAR inter-calibration leads to more
31 conservative estimates of the wind resource.

32

33 Keywords

34 Inter-calibration, offshore wind energy, resource, Synthetic Aperture Radar, Sentinel-1,

35 Envisat

36

37 1. Introduction

38 The Sentinel-1 mission by the European Space Agency (ESA) has secured the availability of
39 Synthetic Apertur Radar (SAR) observations for ocean wind mapping for the years to come.
40 Sentinel-1A (2014–present) and Sentinel-1B (2016–present) are designed for continuation of
41 the previous ESA mission Envisat, which delivered SAR data during 2002-12. SAR
42 instruments are active sensors, which transmit and receive pulses in the microwave range.
43 Properties of the ocean surface waves determine the measured return signal. A C-band SAR
44 sensor is sensitive to waves of the cm-scale, which are typically generated by the
45 instantaneous wind stress at the sea surface.

46

47 Based on scatterometer observations, empirical relationships have been established between
48 radar backscatter from the sea surface and wind speed at the height 10 m. A similar principle
49 can be applied to retrieve wind speeds from SAR observations at a higher spatial resolution
50 and with full coverage over coastal seas (Karagali et al., 2013). Geophysical Model Functions
51 (GMF) for wind speed retrieval at C-band include CMOD4 (Stoffelen and Anderson, 1997),
52 CMOD-IFR2 (Quilfen et al., 1998), CMOD5 (Hersbach et al., 2007), CMOD5.n (Hersbach,
53 2010), CMOD6 and CMOD7 (Stoffelen et al., 2017). The CMOD functions are developed for
54 radar observations with vertical polarization in transmit and receive (VV) and a polarization
55 ratio must be applied in order to compensate for the lower signal at HH (Liu et al., 2013;
56 Mouche et al., 2005; Thompson et al., 1998). A new model function called C_SARMOD2 is
57 developed directly from RADARSAT-2 and Sentinel-1 SAR observations (Lu et al., 2018).

58

59 Wind speed retrievals from Envisat have been compared to in situ observations in different
60 parts of the world (Chang et al., 2015; Doubrawa et al., 2015; Hasager et al., 2015a; 2015b;
61 2011; Takeyama et al., 2013a; 2013b) and evaluations of wind speeds from Sentinel-1 are

62 also published (Ahsbahs et al., 2018; Lu et al., 2018; Monaldo et al., 2016). The Root Mean
63 Square Error (RMSE) of the SAR wind speed with respect to reference data sets is typically
64 less than 2.0 m s^{-1} whereas the bias can vary largely. The temporal and spatial scales of wind
65 data should be considered in any comparison analysis (Hasager et al., 2002). Likewise, care
66 must be taken to compare consistently either the real winds or the Equivalent Neutral Wind
67 (ENW) (Kara et al., 2008; Portabella and Stoffelen, 2009).

68

69 The installed wind power capacity is growing rapidly around the world and plans for new
70 installations offshore are ambitious; particularly in Europe and Asia. In order to produce
71 robust estimates of the wind resource, the highest possible number of independent wind speed
72 observations is needed. The sampling frequency, which can be achieved from polar-orbiting
73 satellites, is poor compared to the sampling frequencies of typical in situ sensors or numerical
74 models. The strength of satellite wind fields lie in the observation of large spatial domains
75 over extensive periods. In order to maximize the number of available satellite wind fields for
76 wind resource assessment, the opportunity to combine data series from different sensors is
77 very attractive. However, effects of sensor-specific characteristics need to be taken into
78 account before the data series can be merged.

79

80 Satellite data merging is performed in connection with Climate Data Records (CDRs) defined
81 as “time series of measurements of sufficient length, consistency and continuity to determine
82 climate variability and change” (National Research Council, 2004). Merged time-series from
83 various sensors and for different physical parameters such as ocean surface winds from
84 scatterometers (Elyouncha and Neyt, 2013; Wentz et al., 2017), ice sheet elevation from
85 altimeters (Khvorostovsky, 2012), and temperature from microwave sounders (Christy et al.,
86 1998) already exist. Although the record of wind retrievals from space is not yet long enough

87 to determine climate variability and change, the community effort is to generate consistent
88 and stable time-series. Inter-calibration ensures consistency between products from different
89 sensors and it can be performed using reference data sets of in situ observations and inter-
90 comparison among different products (Zeng et al., 2015).

91

92 The objective of this paper is to inter-calibrate SAR observations from Envisat and Sentinel-1
93 SAR and combine them to a single data series suitable for wind speed retrieval and resource
94 assessment. Section 2 describes the data sets analyzed and the pre-processing applied. In
95 Section 3, we present a series of initial comparisons between SAR-retrieved wind speeds and
96 ocean buoy observations. A method for inter-calibration of the SAR observations is given in
97 Section 4. In Section 5, comparisons against the reference data set are shown after SAR inter-
98 calibration. The effect of SAR inter-calibration on wind resource estimation is examined in
99 Section 6. Our findings are discussed in Section 7 and conclusions are given in Section 8.

100

101 2. Data and pre-processing

102

103 2.1 Satellite SAR wind maps

104 This analysis is based on Level-1 SAR data from Envisat and Sentinel-1 A/B, which are
105 available from the Copernicus Open Access Hub at <https://scihub.copernicus.eu/>. Our focus is
106 on scenes acquired in ScanSAR mode i.e. the Envisat Wide Swath Mode (WSM) and the
107 Sentinel-1 Interferometric Wide Swath (IW) and Extra Wide Swath (EW) Modes. The swath
108 width is fixed at 400 km for WSM and EW and 250 km for IW whereas the length of scenes
109 is variable. All available products covering the seas of Northern Europe (Figure 1) have been
110 downloaded for the period 2002/08/20 to 2018/05/31. Sentinel-1A products generated after
111 2015/11/25 at 10:40 UTC are processed with a radiometric performance enhancement

112 whereas only some of the scenes acquired during the commissioning phase of Sentinel-1A
113 have been reprocessed (Miranda, 2015). Calibration inconsistencies are therefore still present
114 for the early Sentinel-1A data. The radiometric accuracy of Sentinel-1B observations has been
115 satisfactory, and also compatible with that of Sentinel-1A, since launch (Schwerdt et al.,
116 2017).

117

118 Retrieval of wind speed maps from the Envisat and Sentinel-1 SAR scenes is performed with
119 the SAR Ocean Products System (SAROPS) developed by the Johns Hopkins University,
120 Applied Physics Laboratory and the US National Atmospheric and Oceanographic
121 Administration (NOAA) (Monaldo et al., 2014). The CMOD5.n (Hersbach, 2010) function is
122 chosen for the wind speed inversion and the polarization ratio of Mouche et al. (2005) with
123 incidence angle dependence is applied to the scenes acquired in HH. Regardless of the
124 original resolution of satellite SAR products, we average pixels to a size of 0.5 km prior to the
125 wind retrieval processing to reduce effects of random noise and of surface inclination due to
126 longer-period ocean waves. This is common practice for SAR wind retrievals (Dagestad et al.,
127 2012).

128

129 Because several wind speed and direction pairs may correspond to a single value of
130 backscatter intensity from SAR, information about the wind direction is needed in order to
131 retrieve the wind speed. We obtain the wind directions from the Climate Forecast System
132 Reanalysis (CFSR, <http://nomads.ncdc.noaa.gov/data.php?name=access#cfs-reanal-data>)
133 during 2002-10 and from the Global Forecast System (GFS) at 0.50° resolution during 2010-
134 12 (<http://nomads.ncdc.noaa.gov/data/gfsanl>) and at 0.25° resolution from 2014 onwards
135 (<ftp://ftp.ncep.noaa.gov/pub/data/nccf/com/gfs/prod>). The model outputs are interpolated
136 spatially to match the grid cells of the SAR scenes.

137

138 Land surfaces are masked out during the SAR wind processing using the Global Self-
139 consistent, Hierarchical, High-resolution Geography Database

140 (<http://www.soest.hawaii.edu/pwessel/gshhg/>). Sea ice is detected using the IMS Daily
141 Northern Hemisphere Snow and Ice Analysis

142 (http://nsidc.org/data/docs/noaa/g02156_ims_snow_ice_analysis/). The collection of SAR
143 wind maps used as the starting point for our analyses is available at

144 <https://satwinds.windenergy.dtu.dk/>.

145

146 2.2 Ocean buoy observations

147 Observations from ocean buoys are gathered for the North Sea and part of the North Atlantic
148 for the years 2002 to 2018. To prevent biases, the following criteria are set for buoy stations

149 to be included in this analysis: *i*) a station must deliver data during the period 2006 to 2017 or
150 longer; *ii*) no significant change of the buoy position has occurred over time; and *iii*) the buoy

151 is located at least 10 km from the shoreline. A total of 12 buoy stations live up to the criteria

152 and these datasets are from three institutions: UK MetOffice (personal communication), the

153 Irish Meteorological Service, Met Éireann

154 (<https://erddap.marine.ie/erddap/tabledap/IWBNetwork.html>), and the Bundesamt für

155 Seeschifffahrt und Hydrography, BSH (<http://nwsportal.bsh.de/>).

156

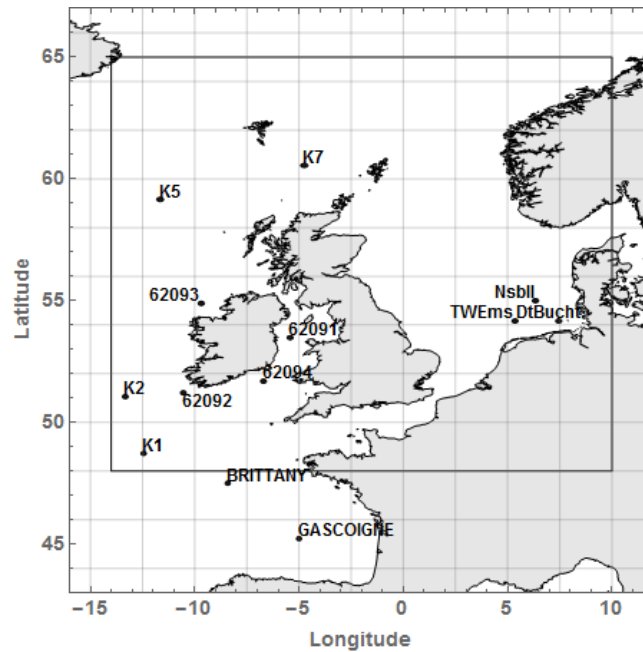
157 The MetOffice and Met Éireann used Ocean Data Acquisition Systems (ODAS) buoys in the
158 early years and some of them have later been replaced with buoys from the manufacturer

159 Fugro. Data from BSH is obtained from light vessels and one moored buoy. Figure 1 shows

160 the buoy locations. Position data from the MetOffice buoys are truncated to 0.1°

161 corresponding to an uncertainty of roughly 10 km on the position. The buoy data are quality

162 controlled by the respective provider and additional inspection of the time series has been
 163 performed in connection with this analysis.



164
 165 *Figure 1. The area investigated and positions of the buoys used in this study. The inner*
 166 *domain shows the area used for SAR inter-calibration in Section 4.*

167
 168 The buoy wind speeds and directions are recorded hourly. Measurement heights vary between
 169 3.5 m and 14 m with the vast majority of the observations at heights lower than 10 m. We
 170 extrapolate to 10-m wind speeds using a logarithmic wind profile:

171
 172
$$u(z) = \frac{u_*}{\kappa} \ln \frac{z}{z_0} \quad (1)$$

173
 174 where $u(z)$ is the wind speed at height z (m s^{-1}), u_* is the friction velocity (m s^{-1}), κ is the von
 175 Kármán constant (~ 0.4), and z_0 is the surface roughness length, which we set to a constant of
 176 0.0002 m.

177

178 The air-sea temperature difference, which is needed to estimate atmospheric stability effects,
179 is typically missing in the buoy data sets. We can thus expect a bias on the 10-m wind speed
180 due to the lack of stability correction of the buoy observations. We assume this bias is
181 constant across the Envisat and Sentinel-1 sensing periods.

182

183 3. Initial comparisons of SAR and buoy observations

184 We first compare the wind speeds retrieved from SAR to wind speed observations from the
185 ocean buoys in the North Sea and North Atlantic. The selection criterion for buoy
186 observations is that their time stamp must be less than 30 minutes from each SAR data
187 acquisition time. To ensure comparability between spatial averaging of the satellite winds and
188 temporal averaging of the buoy observations, we extract the average SAR wind speeds over
189 an area of 10 km by 10 km around the buoy positions. We exclude data points where the SAR
190 or buoy wind speeds are below 0.5 m s^{-1} .

191

192 Buoys provide real wind speeds whereas the SAR wind retrievals are expressed as ENW,
193 which are cleaned for atmospheric stability effects and 0.2 m s^{-1} higher on average (Kara et
194 al., 2008; Portabella and Stoffelen, 2009). Here, we are primarily interested in the consistency
195 between wind retrievals from Envisat and Sentinel-1. Assuming again that the long-term
196 average stability conditions are similar across sensing periods, we can compare the SAR and
197 buoy wind speeds for this purpose without further correction.

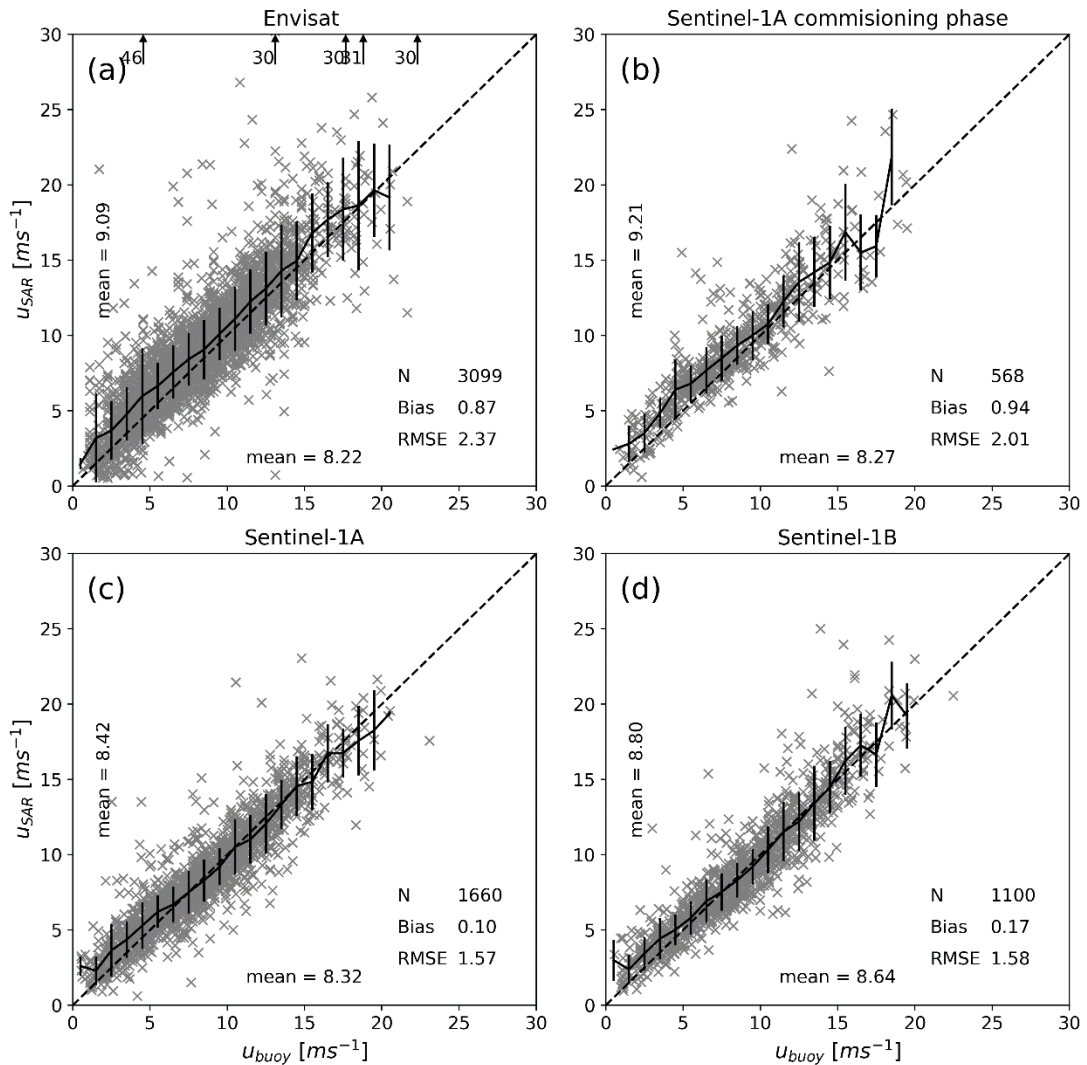
198

199 Figure 2 shows scatterplots of the buoy wind speeds versus the wind speeds retrieved from
200 SAR. A total of 3099 collocated pairs of Envisat and buoy wind speeds are available and the
201 comparison shows a RMSE of 2.37 m s^{-1} . The mean wind speed from Envisat is 0.87 m s^{-1}

202 higher than from the buoy observations. For wind speeds beyond 20 m s^{-1} , the SAR wind
203 speeds are lower than the buoy wind speeds.

204

205 For the subset of Sentinel-1A scenes acquired during the commissioning phase, the
206 comparison show a RMSE of 2.01 m s^{-1} and a positive bias for all wind speed bins up to 16 m
207 s^{-1} . The SAR wind speeds are on average 0.97 m s^{-1} higher than the buoy wind speeds. For the
208 later Sentinel-1A scenes, the RMSE is 1.57 m s^{-1} . Comparisons for Sentinel-1B show almost
209 similar results with RMSE of 1.58 m s^{-1} . For both Sentinel-1 sensors, SAR wind speeds
210 overestimate the buoy wind speeds in the low-wind range. When the wind speed is within the
211 range $7\text{-}17 \text{ m s}^{-1}$, SAR and buoy wind speeds are almost equal and beyond that, the buoy wind
212 speeds are higher. The average bias for Sentinel-1A and B after commissioning is only 0.10-
213 0.17 m s^{-1} and wind speeds from these two sets of SAR observations are very consistent with
214 each other. There is an offset with respect to wind retrievals from Envisat and Sentinel-1A
215 observations during commissioning.



216

217 *Figure 2. Comparisons of wind speeds retrieved from SAR against buoy wind speeds for (a)*

218 *Envisat; (b) Sentinel-1A commissioning phase; (c) Sentinel-1A; and (d) Sentinel-1B.*

219

220 3.1 Wind speed dependence on the wind direction input

221 To examine the effect of the wind direction input chosen for the SAR wind retrieval

222 processing, we repeat the comparisons between SAR and buoy wind speeds using a second

223 set of SAR wind speeds retrieved over each of the buoy stations with observed wind

224 directions from the buoys as input. The buoy wind directions are expected to be more accurate
 225 than the model wind directions initially used for the SAR wind retrieval because *i)* they are
 226 representative for the exact buoy locations, *ii)* they are measured in a consistent manner
 227 across the Envisat and Sentinel-1 sensing periods, and *iii)* they are observed rather than
 228 simulated.

229

230 *Table 1. Summary of comparisons between SAR and buoy wind speeds. The SAR wind speeds*
 231 *are retrieved with wind directions from a model and from buoy observations.*

	Envisat		Sentinel-1A commissioning phase		Sentinel-1A		Sentinel-1B	
	Model	Buoy	Model	Buoy	Model	Buoy	Model	Buoy
Wind direction input								
N	3099	3099	568	568	1660	1660	1100	1100
Bias [m s ⁻¹]	0.87	0.92	0.94	0.92	0.10	0.16	0.17	0.17
RMSE [m s ⁻¹]	2.37	2.37	2.01	1.93	1.57	1.30	1.58	1.26

232

233 Table 1 shows the comparisons of SAR and buoy wind speeds when modelled vs. buoy wind
 234 directions are used to drive the wind speed retrieval from SAR. For Envisat, the RMSE is
 235 unchanged (2.37 m s⁻¹) and the positive bias has increased by 0.05 m s⁻¹ with respect to the
 236 comparison in Figure 2. For all Sentinel-1 data subsets, a small improvement of the RMSE is
 237 seen whereas the bias changes by less than 0.1 m s⁻¹. The offset between winds from Envisat

238 and Sentinel-1 after commissioning remains around 0.8 m s^{-1} so the quality of wind direction
239 inputs cannot explain the offsets in wind speed biases between different SAR sensors.
240 Because we find the lowest RMSE for SAR wind speeds retrieved with buoy wind directions,
241 we use these SAR wind retrievals for the remaining part of Section 3.

242
243 The comparisons presented above all indicate that SAR winds retrieved systematically with
244 CMOD5.n overestimate the observed wind speed at low to moderate wind speeds. The
245 positive bias is larger for Envisat and Sentinel-1 during commissioning than for the later
246 Sentinel-1 data series. At high wind speeds, SAR winds retrieved from Envisat and Sentinel-1
247 during commissioning still overestimate the observed wind speeds whereas wind speeds
248 retrieved from the later Sentinel-1 data series match the reference wind speeds well. The wind
249 speed biases, which we find for the different SAR sensors and periods, cannot be explained
250 by inconsistencies in the ancillary data used to drive the SAR wind retrieval. We therefore
251 turn to examine the effect of different SAR sensing properties on the wind speed accuracy.

252 253 3.2 Wind speed dependence on the radar polarization

254 To investigate the effect of radar polarization on the wind retrieval accuracy, we separate
255 SAR scenes acquired in HH and VV. We can expect the best accuracy at VV polarization
256 since CMOD5.n can be applied directly without a polarization ratio. The majority of SAR
257 scenes in our data set have VV polarization.

258
259 Table 2 shows results of comparisons between SAR and buoy wind speeds at VV and HH
260 polarization for Envisat and Sentinel-1. The RMSE is significantly lower for VV than HH for
261 all data sets except Sentinel-1B. This is as expected due to the added uncertainty introduced
262 by the polarization ratio we apply to SAR observations acquired with HH-polarization (cf.

263 Section 1). A positive bias remains for the VV scenes and there is now an average offset of
 264 0.69-0.73 m s⁻¹ between Envisat and Sentinel-1 retrievals. Envisat scenes acquired in HH
 265 show a large RMSE and a positive bias for all wind speed bins. Sentinel-1 scenes acquired in
 266 HH are associated with a large uncertainty due to the low number of collocated wind speed
 267 samples from SAR and the buoys.

268

269 *Table 2. Summary of comparisons between SAR and buoy wind speeds divided according to*
 270 *sensor and polarization.*

Polarization	Envisat		Sentinel-1A commissioning phase		Sentinel-1A		Sentinel-1B	
	VV	HH	VV	HH	VV	HH	VV	HH
N	2777	322	541	61	1620	42	1089	11
Bias [m s ⁻¹]	0.86	1.43	1.02	0.82	0.13	-1.3	0.17	0.04
RMSE [m s ⁻¹]	2.20	3.56	2.00	3.31	1.56	2.7	1.58	1.44

271

272 3.3 Wind speed dependence on the radar incidence angle

273 Based on the collocated SAR and buoy wind speed pairs analyzed above, we investigate the
 274 dependence on the SAR-buoy wind speed residuals on the radar incidence angle. Visual
 275 inspection of the SAR derived wind fields indicate that wind speeds can vary across the radar
 276 swath even though the radar incidence angle is taken into account during the SAR wind
 277 retrieval. Higher wind speeds typically occur at high incidence angles.

278

279 Figure 3 shows the SAR-buoy wind speed residuals as a function of the radar incidence angle.
280 For Envisat, the average wind speed residuals are lower than 1 m s^{-1} for incidence angles
281 within the range $20\text{-}35^\circ$. Below and above this interval, we see a change of the wind speed
282 residuals as a function of incidence angle. The residuals are always positive indicating higher
283 SAR wind speeds compared to the buoy wind speeds. The standard deviation, represented by
284 the error bars, is very high for incidence angles lower than 20° . At all other incidence angles,
285 the standard deviation is $\pm 2 \text{ m s}^{-1}$ or less.

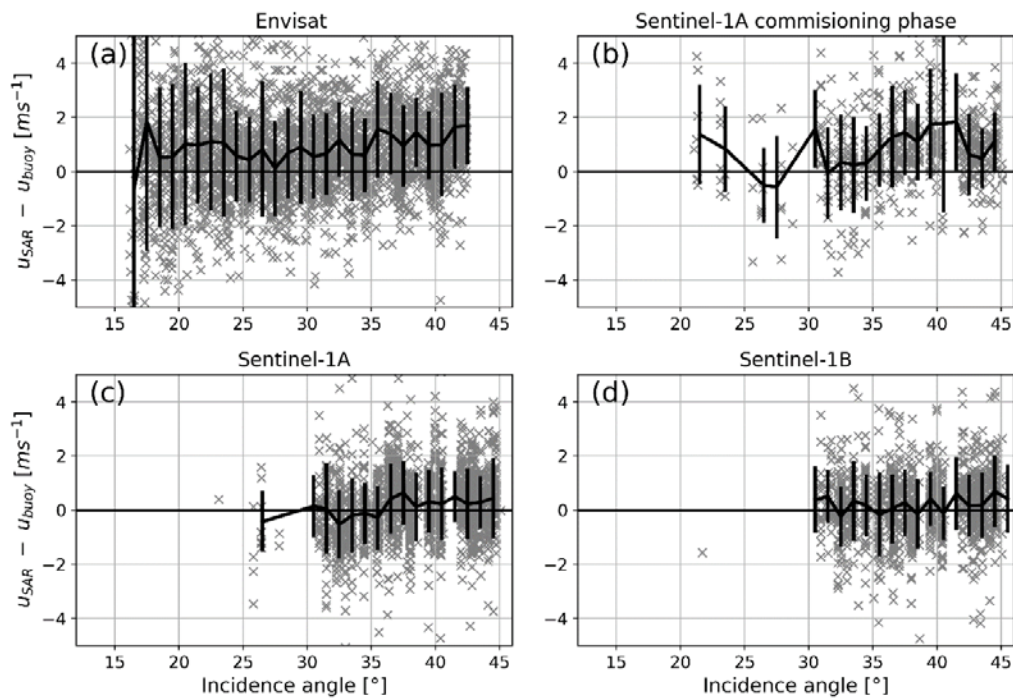
286

287 Most Sentinel-1 samples are obtained within the incidence angle range of $30\text{-}45^\circ$ but a few
288 data points lie within the range of $20\text{-}30^\circ$. During the commissioning phase of Sentinel-1A,
289 we see large fluctuations of the wind speed residuals and error bars of up to $\pm 3 \text{ m s}^{-1}$.

290 Average wind speed residuals for the later Sentinel-1A acquisitions and for Sentinel-1B are
291 always within the range $\pm 1 \text{ m s}^{-1}$ and the standard deviation remains within $\pm 2 \text{ m s}^{-1}$. A
292 trend of slightly increasing wind speed residuals with increasing incidence angles is seen in
293 Figure 3 c) and d).

294

295 Our analyses so far have indicated a consistent difference between wind speed retrievals from
296 Envisat vs. Sentinel-1 A/B, which persists regardless of the wind direction input and the SAR
297 polarization and increases with the SAR incidence angle. To investigate the incidence angle
298 dependence further, we extend the analyses to the Normalized Radar Cross Section (NRCS)
299 input to the SAR wind retrievals.



300

301 *Figure 3. Residuals between SAR and buoy wind speeds as a function of radar incidence*
 302 *angle for (a) Envisat; (b) Sentinel-1A commissioning phase; (c) Sentinel-1A; and (d) Sentinel-*
 303 *1B.*

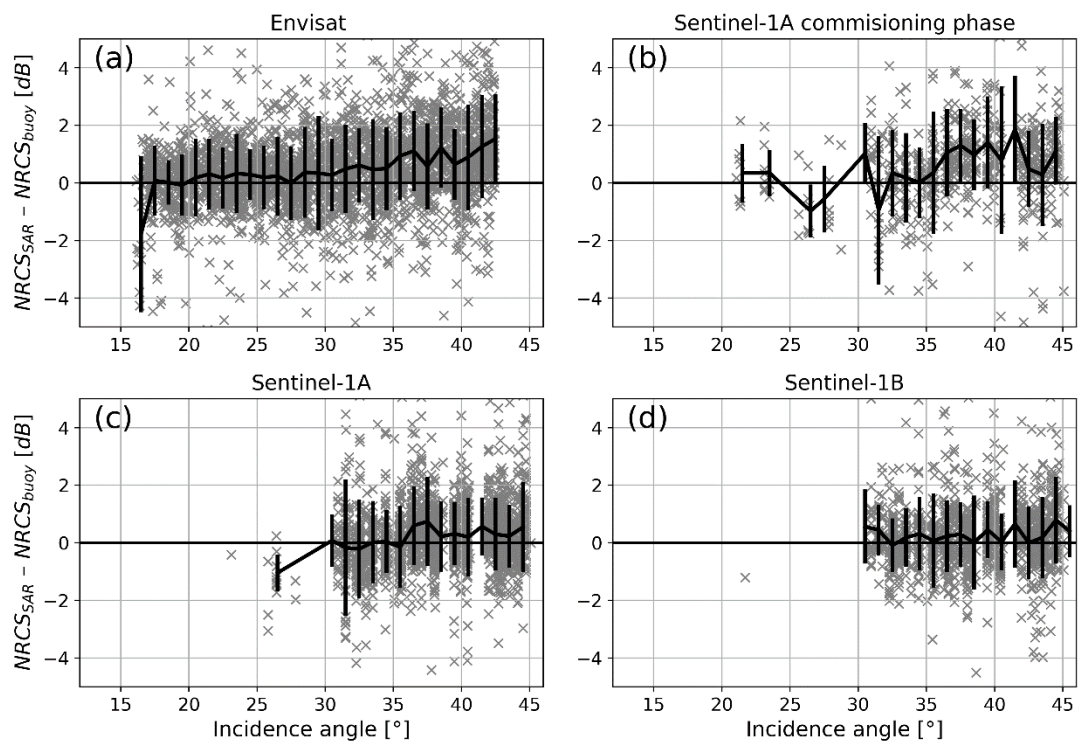
304 3.4 NRCS dependence on the radar incidence angle

305 In the following, we use buoy wind speeds and directions to retrieve the NRCS for different
 306 radar incidence angles. To achieve this, we apply CMOD5.n in forward mode i.e. we use the
 307 buoy wind speed and direction and the radar incidence angle as input and retrieve the NRCS.
 308 We then compare the observed and retrieved NRCS.

309

310 Comparisons of observed and retrieved NRCS from buoy winds are shown in Figure 4. For
 311 Envisat, the residual of NRCS [dB] is very small at low incidence angles and it increases
 312 gradually for incidence angles larger than 20°. The relationship between the incidence angle
 313 and the NRCS residuals in dB space is almost linear. For the Sentinel-1A commissioning
 314 phase, a linear relationship between NRCS residuals and the incidence angle is seen across

315 the interval $32\text{--}41^\circ$ and there are very few data points at lower incidence angles. For Sentinel-
 316 1 A/B, the incidence angle range is smaller and the observed NRCS is higher than for Envisat.
 317 This leads to smaller residuals with respect to the retrieved NRCS and again, we see a linear
 318 increase of NRCS with the incidence angle. The results in Figure 4 suggest that changes of
 319 NRCS residuals with the radar incidence angle is the source of the wind speed biases reported
 320 above. In the following, we present a method for correction of the sensor-specific incidence
 321 angle dependence.



322
 323 *Figure 4. Residuals between measured and retrieved NRCS using buoy wind speeds and*
 324 *directions together with radar incidence angles as input to the simulation for (a) Envisat; (b)*
 325 *Sentinel-1A commissioning phase; (c) Sentinel-1A; and (d) Sentinel-1B.*

326
 327
 328

329 4. SAR inter-calibration

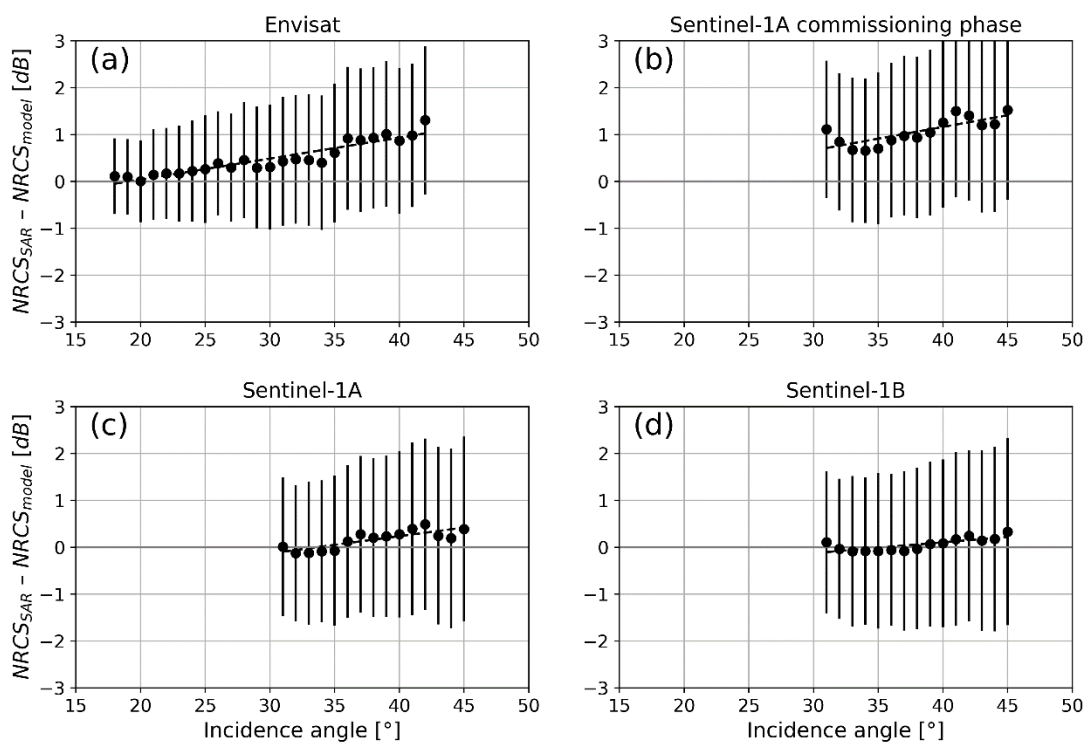
330 Inspired by inter-calibration of scatterometers in Elyouncha and Neyt (2013), where sensors
331 are inter-calibrated using CMOD5.N in forward mode using wind speeds and directions from
332 global circulation models, we calculate sensor-specific corrections of NRCS. These
333 corrections are applied to the NRCS observed by different SAR sensors in order to achieve an
334 inter-calibrated SAR data series.

335
336 The starting point for the inter-calibration is the set of SAR wind fields obtained within the
337 domain shown in Figure 1 with a distance of at least 20 km from the shore. In addition to the
338 10-m wind speed, each data file contains the observed NRCS, radar incidence angle, and look
339 direction as well as wind speeds and directions from a global circulation model (cf. Section
340 2.1). Since model wind speeds and directions are available for all SAR acquisition times and
341 all locations, it is convenient to use these for the inter-calibration analysis to achieve the
342 largest possible number of data points for the correction of NRCS. All the listed data layers
343 are resampled to 10 km grid cells to make the SAR observations more comparable to the
344 resolution of the model data and to reduce our computational effort. Resolution cells with
345 wind speeds from either model or SAR-derived winds below 2 m s^{-1} and above 20 m s^{-1} are
346 filtered out.

347
348 NRCS is retrieved from the model wind speed and direction and the radar viewing geometry
349 in a similar fashion as in Section 3.4. Residuals with respect to the observed NRCS (in dB
350 space) are then calculated within incidence angle bins of 1° and a linear fit is made based on
351 the median values. We split our data set according to sensor, polarization, and scan modes.
352 Additionally, we take into account that the calibration of a sensor can change over time by
353 calculating NRCS-corrections on a monthly basis. For each month, data from the previous full

354 year is used. For the first 12 months a given sensor is in operation, model data covering the
355 same 12 months are used for correction.

356 Figure 5 shows examples of the fitted linear functions for one year of data from Envisat ,
357 Sentinel-1A commissioning phase, Sentinel-1A, and Sentinel-1B. A clear offset is seen for
358 Envisat, which increases with the incidence angle. The NRCS residuals are less pronounced
359 for Sentinel-1A/B.



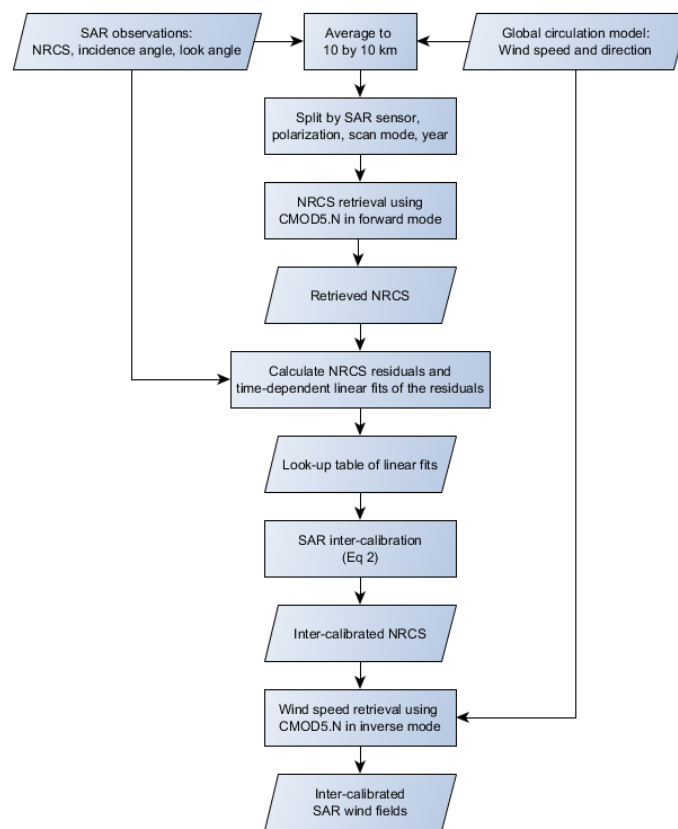
360
361 *Figure 5. Examples showing linear fits to the NRCS residual per incidence angle based on*
362 *one year of data from (a) Envisat (2008-03 to 2009-03); (b) Sentinel-1A commissioning phase*
363 *(2014-11 to 2015-11); (c) Sentinel-1A (2017-04 to 2018-04); and (d) Sentinel-1B (2017-04 to*
364 *2018-04).*

365

366 Subtracting the linear fits from the NRCS observations made by Envisat and Sentinel-1
 367 corrects the bias and the slope of NRCS in dB space:

368
$$\sigma_{IC}^0(\theta) = \sigma^0(\theta) - fit(year, \theta), \quad (2)$$

369 where σ^0 [dB] is the NRCS and θ [°] is the radar incidence angle. The subscript ‘IC’ denotes
 370 that NRCS is now inter-calibrated between the sensors. Figure 6 illustrates the entire
 371 processing chain of the inter-calibration method applied here.



372

373 *Figure 6. Flow chart showing the processing steps of SAR inter-calibration.*

374

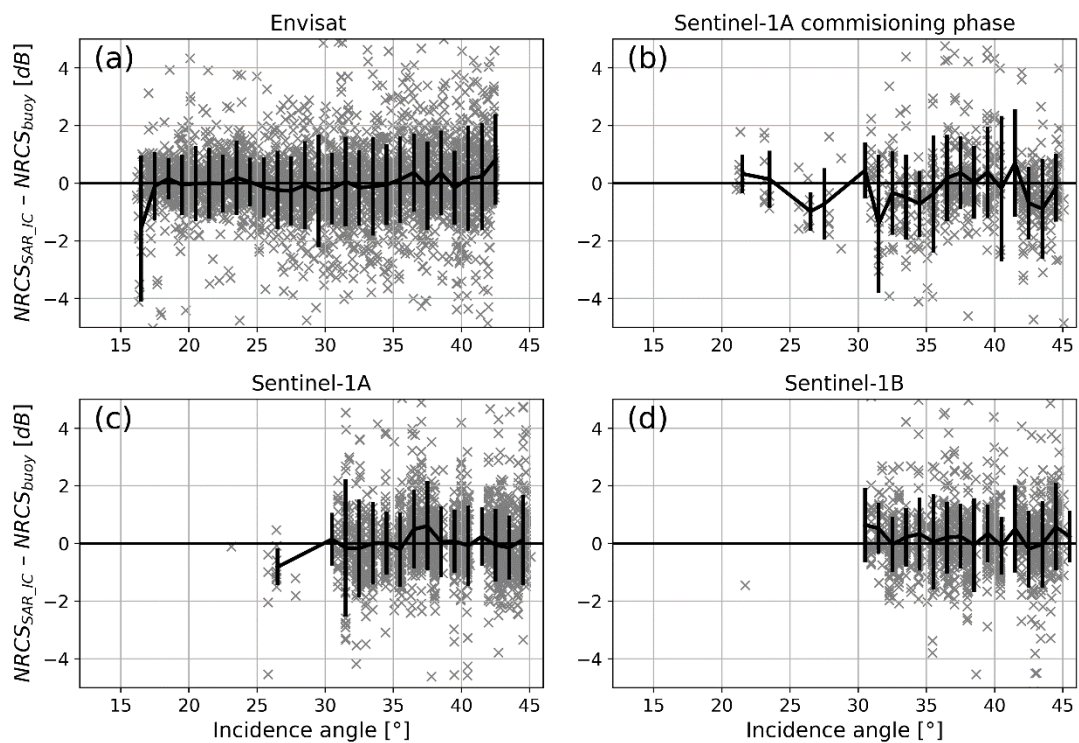
375 5. Comparisons of SAR and buoy observations after inter-calibration

376 The SAR inter-calibration procedure presented above relies solely on global circulation model
 377 wind speeds and directions. We can therefore return to the ocean buoy observations of wind

378 speed and use these as an independent reference data set. In the following, we compare the
379 inter-calibrated NRCS and SAR wind speed retrievals to the buoy observations.

380

381 Figure 7 shows residuals between measured and retrieved NRCS as a function of the radar
382 incidence angle. The plots are comparable to those in Figure 4; the only difference being that
383 the NRCS measured from SAR is now inter-calibrated. As a result, residuals of NRCS are
384 very close to zero for the entire span of incidence angles. It is remarkable how the large
385 residuals that we found initially for Sentinel-1 during the commissioning phase are now
386 reduced to a level similar to that of the later Sentinel-1 data series.



387

388 *Figure 7. Residuals between measured and retrieved NRCS after inter-calibration of NRCS*
389 *for (a) Envisat; (b) Sentinel-1A commissioning phase; (c) Sentinel-1A; and (d) Sentinel-1B.*

390

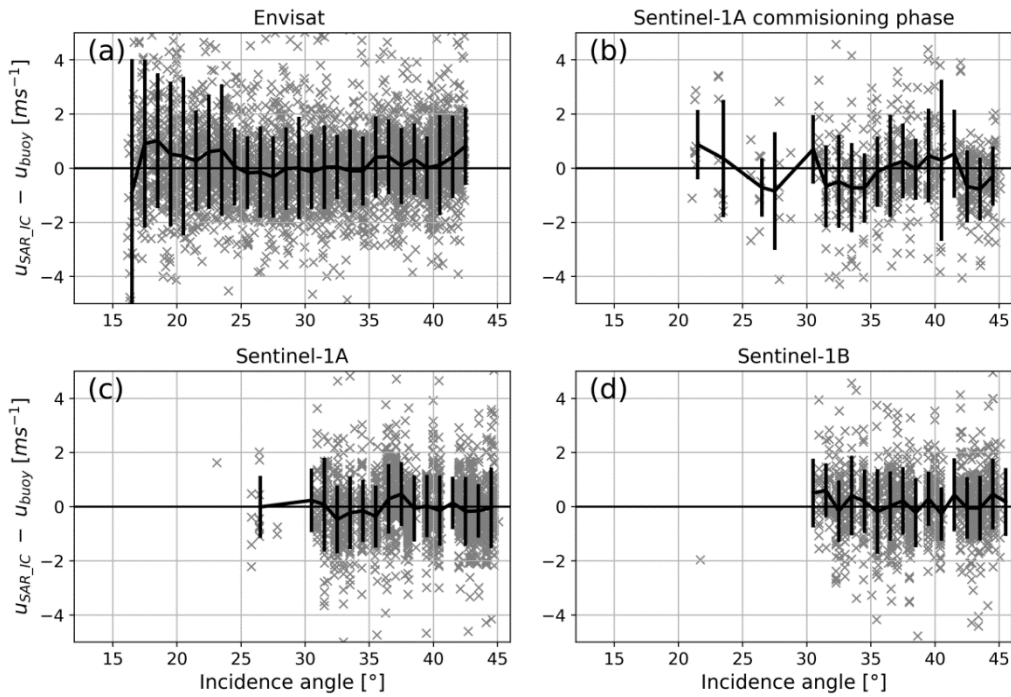
391

392 5.1 Wind speed retrieval from corrected NRCS

393 Once we have inter-calibrated the NRCS, we apply CMOD5.n in inverse mode to retrieve
394 wind speeds once again. Wind speed residuals with respect to the buoy observations are
395 shown as a function of the radar incidence angle in Figure 8. The plots are comparable to
396 plots in Figure 3 made before the SAR inter-calibration. The inter-calibrated SAR
397 observations lead to much smaller wind speed residuals, especially for Envisat, and there is no
398 longer a systematic increase of residuals for increasing incidence angles.

399

400 It is evident from Figure 7 and Figure 8 that our linear correction of the NRCS works best for
401 radar incidence angles above 25° . At very low incidence angles, few or no Sentinel-1 A/B
402 samples are available for fitting a linear function between the radar incidence angle and
403 NRCS residuals. The linear relations found for Envisat at very low incidence angles differ
404 from those found at higher incidence angles. To optimize the wind speed accuracy, we
405 recommend eliminating any data obtained with incidence angles lower than 25° . The
406 following results are calculated with this filter in place.



407
 408 *Figure 8. Residuals between SAR and buoy wind speeds as a function of radar incidence*
 409 *angle after SAR inter-calibration for (a) Envisat; (b) Sentinel-1A commissioning phase; (c)*
 410 *Sentinel-1A; and (d) Sentinel-1B.*

411

412 5.2 Effects of inter-calibration on the wind speed accuracy

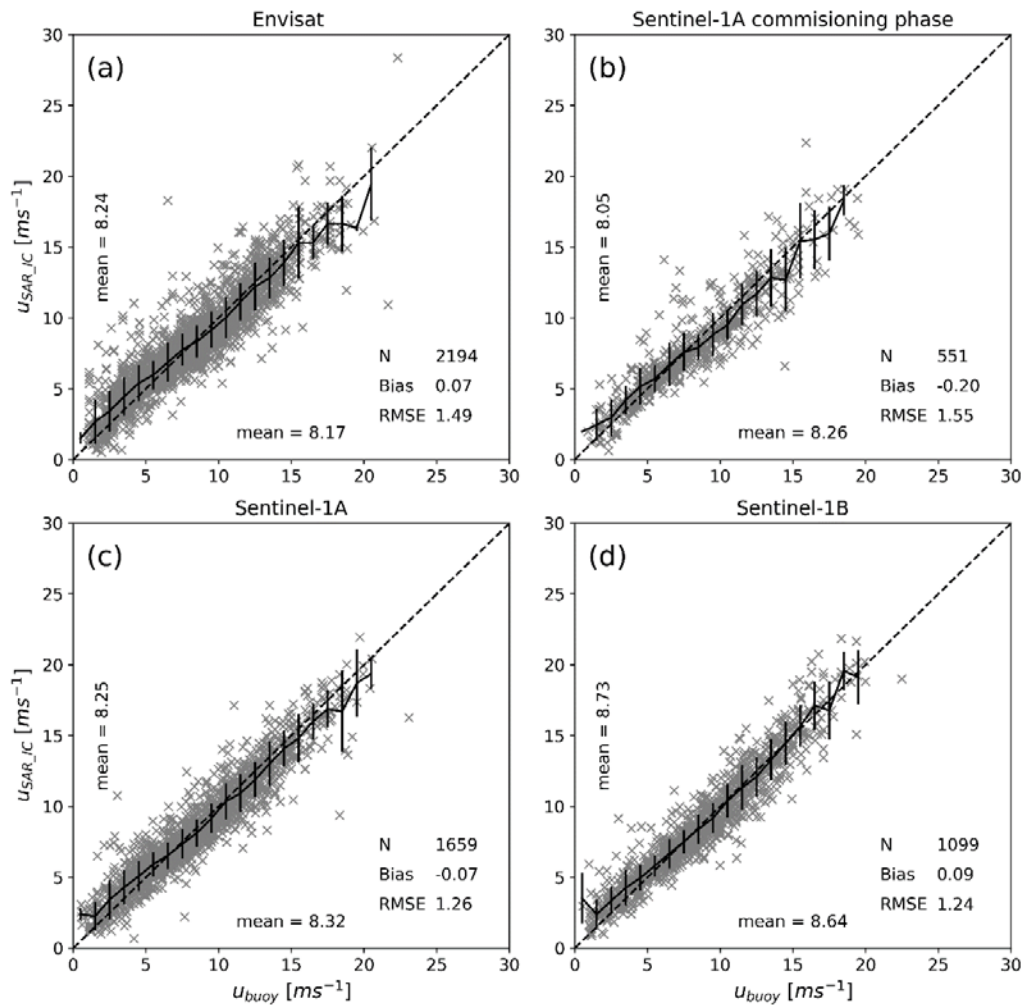
413 In Table 2, we saw large differences in the accuracy of default wind speed retrievals from
 414 SAR observations acquired with VV and HH polarization. The majority of the HH-polarized
 415 SAR scenes in our data set were acquired by Envisat. Table 3 shows how the inter-calibration
 416 has removed any wind speed bias for retrievals based on Envisat observations with both VV
 417 and HH polarization. RMSE is also reduced for both VV and HH but its absolute value
 418 remains higher for scenes acquired with HH polarization.

419

420 *Table 3. Summary of comparisons between SAR and buoy wind speeds retrieved from Envisat*
 421 *observations with VV and HH polarization before and after inter-calibration.*

Polarization	VV		HH	
	Default	Inter-calibrated	Default	Inter-calibrated
N	1978	1978	216	216
Bias [m s ⁻¹]	0.87	0.07	1.42	0.07
RMSE [m s ⁻¹]	1.80	1.44	2.77	1.92

422
 423 Figure 9 shows scatter plots of the buoy and SAR wind speeds per sensor after inter-
 424 calibration of the NRCS. The number of samples given for each plot is a bit lower than in
 425 Figure 2, especially for Envisat. This is due to the filtering of low incidence angles, which
 426 was applied in connection with the inter-calibration. In contrast to the plots in Figure 2, we
 427 now see a consistency between plots for different SAR sensors. All four plots suggest that
 428 SAR winds overestimate buoy observations at low wind speeds up to 7-9 m s⁻¹ and
 429 underestimate with respect to the buoy observations for higher wind speeds.



430
 431 *Figure 9. Comparisons of wind speeds retrieved from inter-calibrated SAR observations*
 432 *against buoy wind speeds for (a) Envisat; (b) Sentinel-1A commissioning phase; (c) Sentinel-*
 433 *1A; and (d) Sentinel-1B.*

434

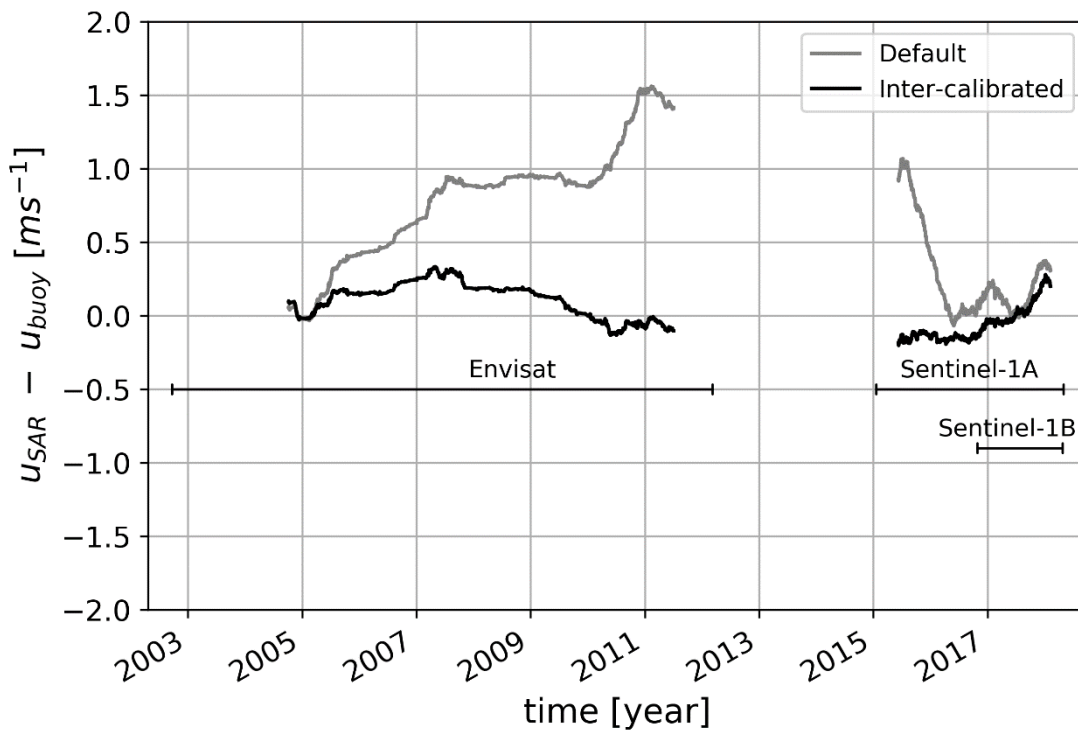
435 In Table 4, we present an overview of statistics per SAR sensor before and after the SAR
 436 inter-calibration and using the same set of samples. The inter-calibration consistently leads to
 437 a lower RMSE and biases that are close to zero for all sensors.

438

439 *Table 4. Summary of comparisons between SAR and buoy wind speeds before and after inter-*
 440 *calibration.*

	Envisat		Sentinel-1A commissioning phase		Sentinel-1A		Sentinel-1B	
	Default	Inter-calibrated	Default	Inter-calibrated	Default	Inter-calibrated	Default	Inter-calibrated
N	2194	2194	551	551	1659	1659	1099	1099
Bias [m s ⁻¹]	0.92	0.07	0.92	-0.20	0.16	-0.07	0.18	0.09
RMSE [m s ⁻¹]	1.92	1.49	1.93	1.55	1.30	1.26	1.26	1.24

441
 442 The effect of SAR inter-calibration on wind speed retrievals over time is illustrated in Figure
 443 10. The plot shows how there is a drift of the SAR wind speed accuracy with respect to
 444 reference measurements at the buoy stations during Envisat’s lifetime. Our correction of
 445 NRCS leads to a significant reduction of wind speed residuals during the entire Envisat era.
 446 For Sentinel-1A/B, we see large wind speed residuals for the first two years of operation,
 447 which include the commissioning phase of the sensors. The SAR inter-calibration efficiently
 448 compensates for wind speed biases so the residuals for Sentinel-1A/B are less than +/-0.2 m s⁻¹
 449 ¹ at any given time. From the beginning of 2016, the residuals between SAR and reference
 450 wind speeds are small and the need for NRCS correction is less pronounced.



451

452 *Figure 10. Residuals of the SAR mean wind speed with respect to buoy observations over*
 453 *time. The grey curve is based on default SAR wind retrievals and the black curve is based on*
 454 *wind retrievals from inter-calibrated SAR observations.*

455

456 Our results indicate that we have successfully removed biases on wind retrievals from the
 457 different SAR sensors. The bias removal is crucial for merging of the wind speeds retrieved
 458 from Envisat and Sentinel-1A/B to a single time series, which is desired for e.g. wind energy
 459 resource assessment. In the following, we will examine the effect of inter-calibration on the
 460 wind resource we can estimate for each of the buoy locations.

461

462 6. Wind resource assessment

463 The principle of satellite based wind resource mapping is similar to that of wind resource
 464 assessment from time series observations e.g. with a meteorological mast (Troen and

465 Petersen, 1989) or from outputs of numerical models (Hahmann et al., 2015). For a given grid
466 cell, a time series of SAR wind samples can be constructed and analyzed statistically. A
467 Weibull function is fitted to the frequency distribution of wind speed bins. The function is
468 defined by a scale parameter, A and a shape parameter, k . From these, the wind power density,
469 E (W m^{-2}) is calculated:

470

$$471 \quad E = \frac{1}{2} \rho A^3 \Gamma\left(1 + \frac{3}{k}\right), \quad (3)$$

472

473 where ρ is the air density (here set to 1.23 kg m^{-3}). Repeating this analysis for each point in a
474 geographical grid will lead to wind resource maps (Badger et al., 2010; Doubrawa et al.,
475 2015; Hasager et al., 2015)

476

477 In order to examine the effect of SAR inter-calibration on wind resource estimates, we
478 calculate the wind power density for each buoy location. The wind power densities are listed
479 in together with the residuals between SAR and buoy wind resources before and after inter-
480 calibration of the SAR data sets. For ten of the 12 buoy locations, we find that the wind power
481 density estimated from SAR after inter-calibration shows a lower bias with respect to the
482 buoy observations. The average numerical deviation from the buoy observations is 20%
483 before and 8% after SAR inter-calibration.

484

485

486

487

488

Table 5. Wind power densities ($W m^{-2}$) for the twelve investigated buoy locations.

Station	N	E_{buoy}	E_{SAR}	E_{SAR_IC}	$E_{SAR} - E_{buoy}$	$E_{SAR_IC} - E_{buoy}$
BRITTANY	735	559	632	545	73	-14
62091	644	506	582	486	76	-20
GASCOIGNE	557	450	466	399	16	-51
K7	496	825	948	784	123	-41
TWEms	475	515	595	501	80	-14
62093	456	638	839	712	201	74
62094	449	500	611	489	111	-11
DtBucht	441	461	565	442	104	-19
NsbII	383	681	598	523	-83	-158
62092	276	514	719	563	205	49
K1	260	778	895	727	117	-51
K5	222	819	1013	885	194	66
K2	109	770	994	872	224	102

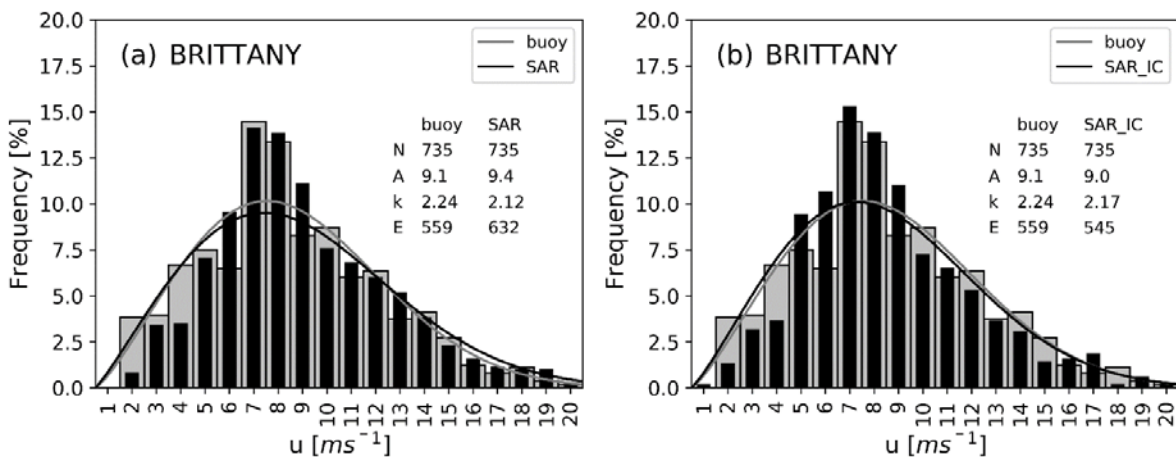
490

491

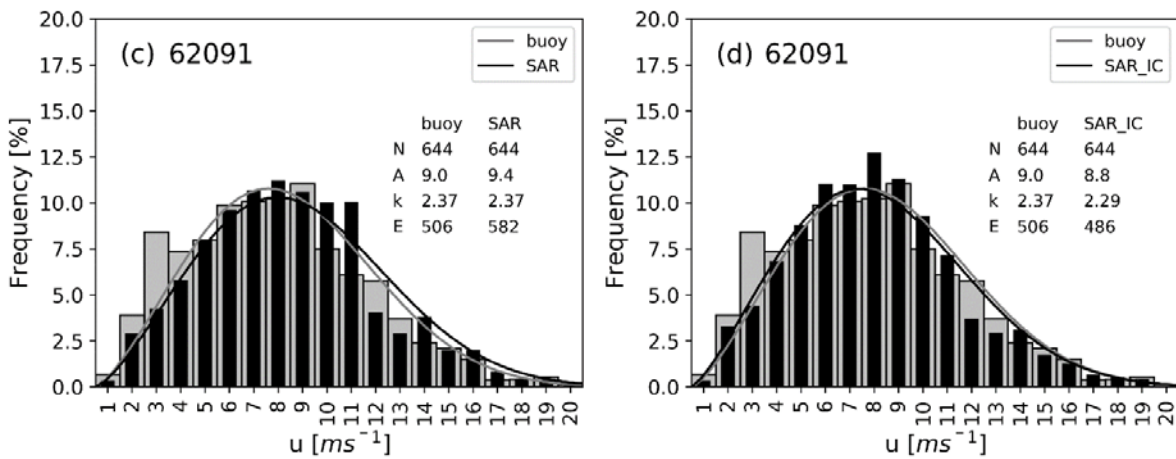
492 It is not clear why the inter-calibration leads to higher residuals at the two sites Gascoigne and
493 Nsbll. One explanation could be that the fitting of a Weibull function introduces some
494 uncertainty to the wind resource estimation. In fact, when we calculate a simple mean value of
495 the wind speed observations, the two stations show better agreement with the reference data
496 after inter-calibration. Other possible reasons for the deviation at the two stations could be
497 issues with the buoy data quality e.g. inaccurate positioning, instrument faults, or biases
498 caused by the vertical extrapolation of wind speed observations.

499

500



501



502

503 *Figure 11. Weibull distributions for the two sites Brittany (a-b) and 62091 (c-d). The Weibull*
 504 *distributions are shown before and after SAR inter-calibration.*

505

506 Figure 11 shows examples of the Weibull distribution for one site exposed to open sea
 507 conditions (Brittany) and another site in the enclosed Irish Sea (62091). The two sites have
 508 the highest number of SAR samples of the sites investigated. The prevailing wind direction
 509 for Brittany is from the south-west. The Weibull fit based on inter-calibrated SAR
 510 observations fits almost perfectly with that of the buoy observations. This is reflected in the
 511 Weibull- k parameter, which changes from 2.12 to 2.17 after inter-calibration. The Weibull-A

512 parameter is also much closer to the buoy observations after inter-calibration and the absolute
 513 residual of the wind power density improves from 73 to 14 W m⁻².

514

515 At the buoy station 62091, prevailing winds are from more southerly directions due to
 516 channeling effects within the Irish Sea. The difference between Weibull curves before and
 517 after inter-calibration of the SAR data is less pronounced than for Brittany. In fact, the values
 518 of Weibull k are identical to the buoy observations before inter-calibration whereas a
 519 difference of 0.08 is found after inter-calibration. As for Brittany, we find that Weibull A and
 520 the wind power density is reduced significantly after the SAR inter-calibration.

521

522 *Table 6. Summary of the bias, RMSE, and MAE of wind resource assessments averaged for*
 523 *the 12 buoy stations investigated. The mean wind speed (U), wind power density (E), Weibull*
 524 *scale (A), and shape (k) parameters are calculated before and after the inter-calibration of*

525 *SAR observations.*

	U [m s ⁻¹]		E [W m ⁻²]		A [m s ⁻¹]		k [-]	
	Default	Inter-calibrated	Default	Inter-calibrated	Default	Inter-calibrated	Default	Inter-calibrated
Bias	0.60	0.05	111	-7	0.49	-0.10	-0.05	-0.06
RMSE	0.67	0.27	138	65	0.57	0.28	0.16	0.12
MAE	0.61	0.21	124	52	0.50	0.26	0.13	0.11

526

527

528 The bias, RMSE, and Mean Absolute Error (MAE) averaged for all 12 buoy stations are
 529 summarized in Table 6. The bias on U is reduced to almost zero and this reduces the bias on
 530 both E and Weibull- A significantly. All three biases change from positive to negative values

531 after the SAR inter-calibration and this leads to more conservative estimates of the wind
532 resource. The bias on Weibull- k remains the same. The RMSE is also reduced for U , E , and
533 Weibull- A indicating a lower uncertainty of wind resource estimates after the SAR inter-
534 calibration.

535

536 7. Discussion

537 Our initial processing of wind speed maps from Envisat and Sentinel-1A/B observations lead
538 to a positive bias for all the SAR sensors investigated but with a large offset between Envisat
539 and Sentinel-1A/B. This is critical if a long time series based on all available SAR
540 observations is desired e.g. for wind resource assessment. The RMSE found in our initial
541 comparisons with buoy observations of wind speed are similar to values found in previous
542 studies based on Envisat (Chang et al., 2015; Doubrawa et al., 2015; Hasager et al., 2015a;
543 2015b; 2011; Takeyama et al., 2013a; 2013b) and Sentinel-1A/B (Ahsbahs et al., 2018; Lu et
544 al., 2018; Monaldo et al., 2016). Our analyses confirm that observations from the two
545 Sentinel-1 sensors A and B lead to wind speeds having almost the same level of accuracy with
546 respect to reference data sets if the commissioning phase of the Sentinel-1A data series is
547 neglected.

548

549 Our analyses show for the first time how observations from different SAR sensors can be
550 inter-calibrated in the same fashion as scatterometer observations are inter-calibrated in
551 connection with CDR development (cf. Section 1). So far, efforts to inter-calibrate SAR
552 observations from different sensors have been limited since relatively few users of the
553 observations see a need for long-term climatological variables. Efforts have instead been
554 dedicated to determining the most suitable GMF for SAR wind retrieval in different areas of
555 the world (Christiansen et al., 2006; Hasager et al., 2015; Takeyama et al., 2013b). Our results

556 indicate that a single GMF cannot retrieve wind speeds from multiple sensors accurately as
557 long as NRCS residuals vary according to sensor type, scan mode, incidence angle, and over
558 the sensor lifetime. It is thus necessary to inter-calibrate the NRCS before wind retrieval
559 processing unless a new GMF is developed specifically for the SAR sensors in question so
560 that inter-calibration is indirectly performed through tuning of the GMF (Lu et al., 2018).

561

562 The inter-calibration method presented here leads to a significant reduction of the offset
563 between wind speed retrievals from Envisat and Sentinel-1A/B observations. After inter-
564 calibration, the average wind speed bias does not exceed $\pm 0.20 \text{ m s}^{-1}$ for any sensor
565 investigated here and the RMSE on wind speeds is less than 1.55 m s^{-1} with respect to ocean
566 buoy observations. For Sentinel-1A/B, we achieve almost zero wind speed bias and a RMSE
567 as low as 1.24 m s^{-1} . The difference between wind resource estimates from SAR and the buoy
568 wind speeds is reduced as a result of inter-calibration for ten of the 12 sites investigated. The
569 inter-calibration removes positive biases from the SAR observations and this leads to lower
570 and more conservative estimates of the wind power density. From an industry perspective, it
571 is important to operate with conservative rather than over-optimistic resource estimates to
572 ensure that potential new wind farms can deliver on feasibility as expected.

573

574 This work relies on several assumptions, which may be investigated further in future research.
575 Wind speed retrievals using CMOD5.n result in the ENW, which is offset from the real wind
576 speed (Kara et al., 2008; Portabella and Stoffelen, 2009). Over the seas of Northern Europe,
577 this offset is found to be smaller than 0.1 m s^{-1} for the height 10 m and it increases for higher
578 levels in the atmosphere (Badger et al., 2016). Our comparisons between SAR and model
579 wind speeds and the calculation of NRCS corrections do not take the offset between ENW
580 and real winds into account. We assume the offset to be constant over time from the Envisat

581 to the Sentinel-1A/B era and so, the impact will be constant for all the SAR data sets
582 investigated. In reality, the atmospheric stability has a seasonal variation as it is temperature-
583 driven. A seasonal inter-calibration analysis would be helpful for quantifying the effect of
584 atmospheric stability.

585

586 In connection with the fitting of linear functions to calculate NRCS corrections, we also
587 assume that the modelled wind speeds will on average converge to the true mean wind speed
588 (both spatially and temporally); otherwise we are adjusting to an offset wind speed.

589 Comparisons between model and in situ wind speeds (not shown here) indicate that the model
590 simulations are indeed consistent with the real wind speeds in the long-term. Our linear fitting
591 is performed for the wind speed interval 2-20 m s⁻¹. A high uncertainty is anticipated for
592 extremely low and high wind speeds due to lower sampling rates and a saturation problem of
593 GMFs at high wind speeds. Work is ongoing in the satellite wind community to resolve
594 extremely high wind speeds thanks to the availability of new cross-polarized SAR sensors
595 (Mouche et al., 2017; Zadelhoff et al., 2014). Further developments of our inter-calibration
596 method might take high wind speeds better into account.

597

598 The spatial and temporal collocation of data sets in our analyses add uncertainties to our
599 findings because: *i*) model simulations and buoy observations are available every hour and the
600 offset in time from the SAR observations may thus be up to 30 minutes; *ii*) the exact geo-
601 location of ocean buoys can be difficult to determine from the metadata provided with the
602 wind speed data; and *iii*) the measurement height for the buoy winds may not be accurate and
603 interpolation to the height of 10 m adds additional uncertainty to wind speed estimates. In
604 order to examine the robustness of our inter-calibration method, it would be valuable to test it
605 for other independent sites where high-quality wind observations are available. The ideal test

606 site would provide offshore wind measurements at the height 10 m together with air-sea
607 temperature differences suitable for atmospheric stability correction.

608

609 The successful inter-calibration of SAR data from the European Space Agency presented here
610 could potentially be extended to cover other SAR sensors and scan modes. As an example,
611 long C-band SAR data series have been acquired by Radarsat-1/2, which is soon to be
612 continued with the Radarsat Constellation Mission. Sensors operating at X-band or L-band
613 represent other possible extensions of the data series investigated here. An added benefit of
614 using SAR observations from a variety of sensors in combination would be that diurnal wind
615 speed variability can be better resolved.

616

617 At present, the calibration of individual SAR sensors is the responsibility of different space
618 agencies and it is typically governed by different requirements. The method for inter-
619 calibration described here can be applied by any end user of SAR data and it is thus promising
620 for inter-calibration of multiple SAR data sets obtained in the past, present and future.
621 Potentially, an inter-calibrated long-term record of SAR wind speeds could be established and
622 offered through publicly available data portals. This would facilitate the best possible
623 accuracy on long-term average wind speeds offshore for many applications including wind
624 energy resource assessment.

625

626 8. Conclusion

627 We have presented a method for inter-calibration of SAR observations with the purpose of
628 constructing a long-term record of wind speed retrievals from SAR. Correction of the NRCS
629 prior to wind retrieval processing efficiently removes biases on wind speeds from Envisat and
630 Sentinel-1A/B observations. The correction varies according to the SAR sensor, scan mode,

631 radar incidence angle, and also over the sensor lifetime. The inter-calibration leads to a
632 significant reduction of wind speed biases and uncertainties expressed through the RMSE.
633 Wind resource estimates become more conservative as a result of the SAR inter-calibration.
634 Our successful calculation of a long-term wind speed record from SAR observations is
635 promising and has a potential for extension using other SAR sensors from the past, present
636 and future. Ultimately, this could lead to establishment of a new derived product offering
637 long-term SAR wind data for wind energy resource assessment and other applications.

638

639 Acknowledgements

640 This work received funding from the EU H2020 program under grant agreement no. 730030
641 (CEASELESS project).

642

643 References

644 Ahsbahs, T., Badger, M., Karagali, I., Larsén, X.G., 2017. Validation of Sentinel-1A SAR
645 coastal wind speeds against scanning LiDAR. *Remote Sens.* 9.

646 <https://doi.org/10.3390/rs9060552>

647 Ahsbahs, T., Badger, M., Volker, P., Hansen, K.S., Hasager, C.B., 2018. Applications of
648 satellite winds for the offshore wind farm site Anholt. *Wind Energy Sci.* 3, 573–588.

649 <https://doi.org/10.5194/wes-2018-2>

650 Badger, M., Badger, J., Nielsen, M., Hasager, C.B., Peña, A., 2010. Wind Class Sampling of
651 Satellite SAR Imagery for Offshore Wind Resource Mapping. *J. Appl. Meteorol.*

652 *Climatol.* <https://doi.org/10.1175/2010JAMC2523.1>

653 Badger, M., Peña, A., Hahmann, A.N., Mouche, A.A., Hasager, C.B., 2016. Extrapolating
654 satellite winds to turbine operating heights. *J. Appl. Meteorol. Climatol.* 55.

655 <https://doi.org/10.1175/JAMC-D-15-0197.1>

656 Chang, R., Zhu, R., Badger, M., Hasager, C., Xing, X., Jiang, Y., 2015. Offshore Wind
657 Resources Assessment from Multiple Satellite Data and WRF Modeling over South
658 China Sea. *Remote Sens.* 7, 467–487. <https://doi.org/10.3390/rs70100467>

659 Christiansen, M.B., Koch, W., Horstmann, J., Hasager, C.B., Nielsen, M., 2006. Wind
660 resource assessment from C-band SAR. *Remote Sens. Environ.* 105, 68–81.

661 Christy, J.R., Spencer, R.W., Lobl, E.S., 1998. Analysis of the merging procedure for the
662 MSU daily temperature time series. *J. Clim.* 11, 2016–2041.
663 <https://doi.org/10.1175/1520-0442-11.8.2016>

664 Dagestad, K.-F., Horstmann, J., Mouche, A., Perrie, W., Shen, H., Zhang, B., Li, X.,
665 Monaldo, F., Pichel, W., Lehner, S., Badger, M., Hasager, C.B., Furevik, B., Foster,
666 R.C., Falchetti, S., Caruso, M., Vachon, P., 2012. Wind retrieval from synthetic aperture
667 radar - an overview, in: *Proceedings of SEASAR 2012 Advances in SAR Oceanography*,
668 Tromsø Norway.

669 Doubrawa, P., Barthelmie, R.J., Pryor, S.C., Hasager, C.B., Badger, M., Karagali, I., 2015.
670 Satellite winds as a tool for offshore wind resource assessment: The Great Lakes Wind
671 Atlas. *Remote Sens. Environ.* 168. <https://doi.org/10.1016/j.rse.2015.07.008>

672 Elyouncha, A., Neyt, X., 2013. C-band satellite scatterometer intercalibration. *IEEE Trans.*
673 *Geosci. Remote Sens.* 51, 1478–1491. <https://doi.org/10.1109/TGRS.2012.2217381>

674 Hahmann, A.N., Vincent, C.L., Peña, A., Lange, J., Hasager, C.B., 2015. Wind climate
675 estimation using WRF model output: Method and model sensitivities over the sea. *Int. J.*
676 *Climatol.* 35, 3422–3439. <https://doi.org/10.1002/joc.4217>

677 Hasager, C.B., Badger, M., Nawri, N., Furevik, B.R., Petersen, G.N., Bjornsson, H., Clausen,
678 N.-E., 2015a. Mapping Offshore Winds Around Iceland Using Satellite Synthetic
679 Aperture Radar and Mesoscale Model Simulations. *IEEE J. Sel. Top. Appl. Earth Obs.*
680 *Remote Sens.* 8. <https://doi.org/10.1109/JSTARS.2015.2443981>

681 Hasager, C.B., Badger, M., Peña, A., Larsén, X.G., Bingöl, F., 2011. SAR-based wind
682 resource statistics in the Baltic Sea. *Remote Sens.* 3. <https://doi.org/10.3390/rs3010117>

683 Hasager, C.B., Dellwik, E., Nielsen, M., Furevik, B., 2002. Validation of ERS-2 SAR
684 offshore wind-speed maps in the North Sea. *Int. J. Remote Sens.*

685 Hasager, C.B., Mouche, A., Badger, M., Bingöl, F., Karagali, I., Driesenaar, T., Stoffelen, A.,
686 Peña, A., Longépé, N., 2015b. Offshore wind climatology based on synergetic use of
687 Envisat ASAR, ASCAT and QuikSCAT. *Remote Sens. Environ.* 156.
688 <https://doi.org/10.1016/j.rse.2014.09.030>

689 Hasager, C.B., Mouche, A., Badger, M., Bingöl, F., Karagali, I., Driesenaar, T., Stoffelen, A.,
690 Peña, A., Longépé, N., 2015. Offshore wind climatology based on synergetic use of
691 Envisat ASAR, ASCAT and QuikSCAT. *Remote Sens. Environ.* 156, 247–263.
692 <https://doi.org/10.1016/j.rse.2014.09.030>

693 Hersbach, H., 2010. Comparison of C-Band Scatterometer CMOD5.N Equivalent Neutral
694 Winds with ECMWF. *J. Atmos. Ocean. Technol.* 27, 721–736.
695 <https://doi.org/10.1175/2009JTECHO698.1>

696 Hersbach, H., Stoffelen, A., de Haan, S., 2007. An improved C-band scatterometer ocean
697 geophysical model function: CMOD5. *J. Geophys. Res.* 112, 16 pp.

698 Kara, A.B., Wallcraft, A.J., Bourassa, M.A., 2008. Air-sea stability effects on the 10 m winds
699 over the global ocean: Evaluations of air-sea flux algorithms. *J. Geophys. Res. Ocean.*
700 113, 1–14. <https://doi.org/10.1029/2007JC004324>

701 Karagali, I., Larsén, X., Badger, M., Peña, A., Hasager, C., 2013. Spectral Properties of
702 ENVISAT ASAR and QuikSCAT Surface Winds in the North Sea. *Remote Sens.* 5,
703 6096–6115. <https://doi.org/10.3390/rs5116096>

704 Khvorostovsky, K.S., 2012. Merging and analysis of elevation time series over greenland ice
705 sheet from satellite radar altimetry. *IEEE Trans. Geosci. Remote Sens.* 50, 23–36.

706 <https://doi.org/10.1109/TGRS.2011.2160071>

707 Liu, G., Yang, X., Li, X., Zhang, B., Pichel, W., Li, Z., Zhou, X., 2013. A Systematic
708 Comparison of the Effect of Polarization Ratio Models on Sea Surface Wind Retrieval
709 From C-Band Synthetic Aperture Radar. *IEEE J. Sel. Top. Appl. Earth Obs. Remote*
710 *Sens.* 6, 1100–1108. <https://doi.org/10.1109/JSTARS.2013.2242848>

711 Lu, Y., Zhang, B., Perrie, W., Mouche, A.A., Li, X., Wang, H., 2018. A C-Band geophysical
712 model function for determining coastal wind speed using synthetic aperture radar. *IEEE*
713 *J. Sel. Top. Appl. Earth Obs. Remote Sens.* 11, 2417–2428.
714 <https://doi.org/10.1109/JSTARS.2018.2836661>

715 Miranda, N., 2015. S-1A TOPS Radiometric Calibration Refinement # 1.

716 Monaldo, F., Jackson, C., Li, X., Pichel, W.G., 2016. Preliminary Evaluation of Sentinel-1A
717 Wind Speed Retrievals. *IEEE J. Sel. Top. Appl. Earth Obs. Remote Sens.* 9, 2638–2642.
718 <https://doi.org/10.1109/JSTARS.2015.2504324>

719 Monaldo, F.M., Li, X., Pichel, W.G., Jackson, C.R., 2014. Ocean Wind Speed Climatology
720 from Spaceborne SAR Imagery. *Bull. Am. Meteorol. Soc.* 95, 565–569.
721 <https://doi.org/10.1175/BAMS-D-12-00165.1>

722 Mouche, A.A., Chapron, B., Zhang, B., Husson, R., 2017. Combined Co- and Cross-Polarized
723 SAR Measurements Under Extreme Wind Conditions. *IEEE Trans. Geosci. Remote*
724 *Sens.* 55, 6746–6755. <https://doi.org/10.1109/TGRS.2017.2732508>

725 Mouche, A.A., Hauser, D., Daloze, J.F., Guerin, C., 2005. Dual-polarization measurements at
726 C-band over the ocean: Results from airborne radar observations and comparison with
727 ENVISAT ASAR data. *IEEE Trans. Geosci. Remote Sens.* 43, 753–769.

728 National Research Council, 2004. *Climate Data Records from Environmental Satellites:*
729 *Interim Report.* The National Academies Press, Washington DC.
730 <https://doi.org/10.17226/10944>

731 Portabella, M., Stoffelen, a., 2009. On Scatterometer Ocean Stress. *J. Atmos. Ocean.*
732 *Technol.* 26, 368–382. <https://doi.org/10.1175/2008JTECHO578.1>

733 Quilfen, Y., Chapron, B., Elfouhaily, T., Katsaros, K., Tournadre, J., 1998. Observation of
734 tropical cyclones by high-resolution scatterometry. *J. Geophys. Res.* 103, 7767–7786.

735 Schwerdt, M., Schmidt, K., Ramon, N.T., Klenk, P., Yague-Martinez, N., Prats-Iraola, P.,
736 Zink, M., Geudtner, D., 2017. Independent system calibration of sentinel-1B. *Remote*
737 *Sens.* 9, 1–34. <https://doi.org/10.3390/rs9060511>

738 Stoffelen, A., Anderson, D.L.T., 1997. Scatterometer data interpretation: Estimation and
739 validation of the transfer function CMOD4. *J. Geophys. Res.* 102, 5767–5780.

740 Stoffelen, A., Verspeek, J.A., Vogelzang, J., Verhoef, A., 2017. The CMOD7 Geophysical
741 Model Function for ASCAT and ERS Wind Retrievals. *IEEE J. Sel. Top. Appl. Earth*
742 *Obs. Remote Sens.* 10, 2123–2134. <https://doi.org/10.1109/JSTARS.2017.2681806>

743 Takeyama, Y., Ohsawa, T., Kozai, K., Hasager, C.B., Badger, M., 2013. Comparison of
744 geophysical model functions for SAR wind speed retrieval in japanese coastal waters.
745 *Remote Sens.* 5. <https://doi.org/10.3390/rs5041956>

746 Takeyama, Y., Ohsawa, T., Kozai, K., Hasager, C.B., Badger, M., 2013. Effectiveness of
747 WRF wind direction for retrieving coastal sea surface wind from synthetic aperture
748 radar. *Wind Energy* 16, 865–878.

749 Takeyama, Y., Ohsawa, T., Kozai, K., Hasager, C.B., Badger, M., 2010. Effect of Wind
750 Direction on ENVISAT ASAR Wind Speed Retrieval, in: *Proceedings (CD-ROM).*
751 *Techno-Ocean Network*, p. 8.

752 Thompson, D., Elfouhaily, T., Chapron, B., 1998. Polarization ratio for microwave
753 backscattering from the ocean surface at low to moderate incidence angles. pp. 1671–
754 1676.

755 Troen, I., Petersen, E.L., 1989. *European Wind Atlas*. Risø National Laboratory, Roskilde,

756 Denmark.

757 Zadelhoff, G.J. Van, Stoffelen, A., Vachon, P.W., Wolfe, J., Horstmann, J., Belmonte Rivas,
758 M., 2014. Retrieving hurricane wind speeds using cross-polarization C-band
759 measurements. *Atmos. Meas. Tech.* 7, 437–449. <https://doi.org/10.5194/amt-7-437-2014>

760 Zeng, Y., Su, Z., Calvet, J.C., Manninen, T., Swinnen, E., Schulz, J., Roebeling, R., Poli, P.,
761 Tan, D., Riihelä, A., Tanis, C.M., Arslan, A.N., Obregon, A., Kaiser-Weiss, A., John,
762 V.O., Timmermans, W., Timmermans, J., Kaspar, F., Gregow, H., Barbu, A.L.,
763 Fairbairn, D., Gelati, E., Meurey, C., 2015. Analysis of current validation practices in
764 Europe for space-based climate data records of essential climate variables. *Int. J. Appl.*
765 *Earth Obs. Geoinf.* 42, 150–161. <https://doi.org/10.1016/j.jag.2015.06.006>

766